Journal of Molecular Structure 1047 (2013) 344–357

Contents lists available at SciVerse ScienceDirect

Journal of Molecular Structure

journal homepage: www.elsevier.com/locate/molstruc

Fundamental insights into conformational stability and orbital interactions of antioxidant (+)-catechin species and complexation of (+)-catechin with zinc(II) and oxovanadium(IV)

Nuttawisit Yasarawan [a], Khajadpai Thipyapong [a,*], Somsak Sirichai [a,b], Vithaya Ruangpornvisuti [c]

[a] Department of Chemistry, Faculty of Science, Burapha University, Chonburi 20131, Thailand
[b] Center of Excellence for Innovation in Chemistry, Faculty of Science, Burapha University, Chonburi 20131, Thailand
[c] Department of Chemistry, Faculty of Science, Chulalongkorn University, Bangkok 10330, Thailand

HIGHLIGHTS

- Electronic behaviors of various (+)-catechin species were theoretically studied.
- Preferential deprotonation occurs successively at C3′-, C5-, C7- and C4′-OH groups.
- The pK_a value predicted for the most acidic OH group agrees well with previous work.
- Hydrogen radical formation is favored at high pH value.
- Complexation with either zinc(II) or oxovanadium(IV) prefers the 1:1 stoichiometry.

GRAPHICAL ABSTRACT

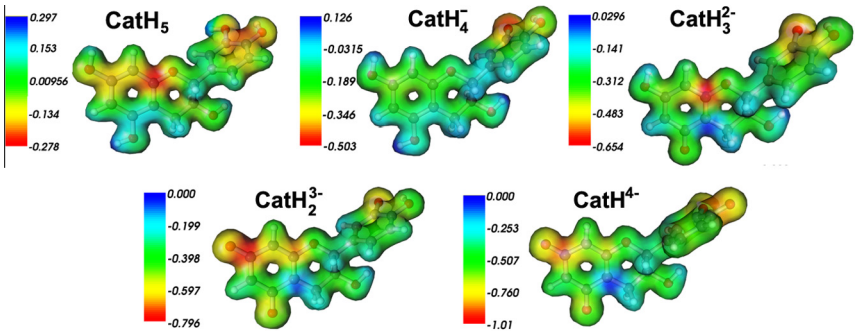

ARTICLE INFO

Article history:
Received 18 April 2013
Received in revised form 20 May 2013
Accepted 20 May 2013
Available online 28 May 2013

Keywords:
Catechin
Antioxidants
Flavanols
Flavonoids
DFT
pK_a

ABSTRACT

Conformational stability of (+)-catechin species in water has been examined with density functional theory, associated with the polarizable continuum model (PCM) of solvation. Factors such as electron delocalization, lone-pair electron donation and intramolecular hydrogen bonding substantially contribute to the conformational stabilization. Upon deprotonation, the HOMO and LUMO energies for (+)-catechin are both elevated; the energy gaps for the deprotonated species are narrower than the energy gap for the neutral species. The preferential deprotonation occurs at the C3′-, C5-, C7- and C4′-OH groups successively. The pK_a value at 9.3 predicted for the most acidic OH group agrees well with previous experimental data; however the values are overestimated for the less acidic OH groups due to limitations of the PCM for charged solutes and/or complex nature of true deprotonation pathways. Formation of hydrogen radicals should be promoted at high pH values following the bond dissociation enthalpies. Complexation of (+)-catechin with either zinc(II) or oxovanadium(IV) is favored at the 1:1 metal-to-ligand (M:L) mole ratio, with the oxovanadium(IV) complex showing higher reaction preference. At M:L = 1:2, formation of two isomeric complexes are plausible for each type of metal ion. Effects of stoichiometry and isomerism on the computational spectral features of the possibly formed metal complexes have been described.

1. Introduction

(+)-Catechin is a naturally occurring polyphenolic compound belonging to a subclass, known as flavan-3-ol, in the flavonoid family. Such the compound is found in various plants and foods derived from plants (e.g., tea, cocoa, berries, and red wines), and is also well known for its satisfactory antioxidant activity, providing the protection against diseases directly or partially involving accumulation of free radicals in the body, e.g. cancers, aging, diabetes, neurodegenerative and cardiovascular diseases [1–5]. The antioxidant activity of (+)-catechin arises from its ability to scavenge

* Corresponding author. Tel.: +66 38 103 069; fax: +66 38 393 494.
E-mail address: khajadpa@buu.ac.th (K. Thipyapong).

0022-2860/$ - see front matter © 2013 Elsevier B.V. All rights reserved.
http://dx.doi.org/10.1016/j.molstruc.2013.05.038

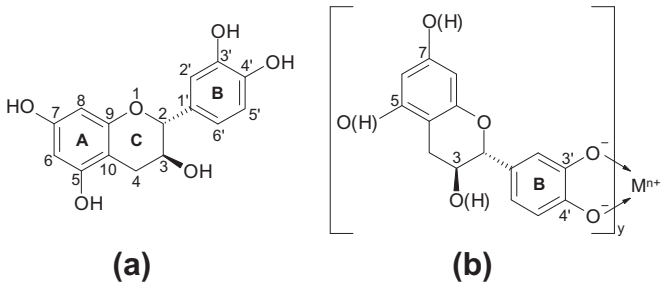

Fig. 1. Schematic representation of **(a)** (+)-catechin and **(b)** the complex of (+)-catechin with $M^{n+} = Zn^{2+}$ or VO^{2+}, and $y = 1$ or 2. The labeling system is included for the three-ring skeleton. Five protic sites are at the C5, C7, C3′ and C4′ hydroxyl (OH) groups. Two donor oxygen atoms responsible for the metal ion chelation are attached to C3′ and C4′.

reactive oxygen and nitrogen species produced during the cellular oxidation processes. As shown in Fig. 1a, a molecule of neutral (+)-catechin denoted as $CatH_5$ consists of three six-membered rings: the resorcinol ring (A), the catechol ring (B) and the hydroxydihydropyran ring (C). The rings A and B are aromatic moieties while the ring C is a non-aromatic heterocyclic moiety. With five hydroxyl (OH) groups attached to the C3′, C4′, C5 and C7 carbon atoms, (+)-catechin is regarded as a polyprotic compound, and the antioxidant activity relies on either the hydrogen or electron donation from these OH groups to the reactive free radicals [6–8]. It is noteworthy to mention that the OH group at C3 is technically not acidic as it is a non-dissociable aliphatic alcohol functional group. In aqueous solution at a specified pH, the protonation–deprotonation equilibria of (+)-catechin could play a key role in the redox phenomena and in vitro antioxidant activity as reported in the previous studies [9–11]. This is important for the in vivo antioxidant activity of (+)-catechin as the pH values in the human body vary in quite a broad range, for example, the normal blood pH and tissue fluids is 7.4 while the stomach pH value is close to 1 [7]. In principle, the most preferential deprotonation sequence of (+)-catechin depends on the pK_a values assigned to the individual OH groups. Due to the phenolic nature of (+)-catechin, the pK_a value of around 9–10 is expected for the most acidic OH group. Formerly, determination of the pK_a values for (+)-catechin were carried out using electrochemical and spectroscopic methods [12–16], and the value of about 9 was obtained quite precisely for the most acidic OH group. On the other hand, uncertainties of the pK_a values for the less acidic OH groups seem to be large due to either difficulties in detection or small differences between these values. Assigning the pK_a values to the four OH groups of (+)-catechin is even more challenging as the molecular origins of the preferential deprotonation sequence need to be well comprehended. Practically, comparisons between the experimental data obtained from (+)-catechin and those from various catechol-based or resorcinol-based model compounds were made in order that the acidity contributions from the two rings in (+)-catechin could be identified more accurately [13–15]. In some studies, the most acidic OH group on (+)-catechin was assigned to the C3′-OH group on the ring B [14,15]; however the OH group at C4′ was also claimed to be the most acidic group [7,17]. In this case, the high-level quantum mechanical methods based on density functional theory (DFT) have been found necessary in the validation of the acidity assignment to different OH groups. By such the theoretical methods, the deprotonation sequence as well as the molecular stability of various (+)-catechin species can be explicitly described, providing profound insights into the dependence of the structural and electronic behaviors of the antioxidant molecule on the deprotonation processes. Essentially, any single deprotonation step may cause significant changes in the conformation of the deprotonated molecule due to the reorganization of its electronic charges. Such the structural change can possibly have much influence on the subsequent deprotonation steps and hence the overall deprotonation pathway. Therefore, in the present study, the most stable conformations for the neutral and deprotonated (+)-catechin species need to be determined by means of the full molecular geometry optimization. The molecular properties involving conformational stability and reactivity such as charge density distributions, bond orbital interactions and frontier molecular orbital energies, have been well described for all (+)-catechin species. Interestingly, it has been realized that particular transition metal ions such as chromium(III) [18–21], zinc(II) [22–28] or vanadium(IV) [23,27,29–31] are active in reducing blood glucose levels both in vitro and in vivo. A great deal of work has been carried out to investigate the insulin-mimetic activity of such the transition metal ions, particularly in the forms of ligand–metal complexes as the carbohydrate and lipid metabolic activities are frequently regulated by the biochemically active complexes formed by proteins and metal ions [18,20,28,32,33]. Finding more appropriate ligands for the production of antidiabetic complexes is also of general significance in pharmacological context. (+)-Catechin could serve as a potential candidate for the ligand to be used in the preparation of therapeutic metal complexes similar to the other biologically friendly flavonoids [34,35]. This approach may allow the development of compounds with combined antidiabetic and antioxidant properties as well. Interestingly, a significant number of metal complexes of flavonoids have been reported as exhibiting greater antioxidant activity than their free ligand counterparts [35]. In terms of drug release, the insulin-mimetic metal ions bound to ligands are expected to be released in a controlled manner to bloodstream; therefore in this case, the glucose-lowering effect would vary with stability of the complexes. In the present study, the effects of metal–ligand stoichiometry and the chelation configuration on the stability of the complexes formed by (+)-catechin and the insulin-mimetic transition metal ions such as zinc(II) and oxovanadium(IV) have been investigated employing the DFT computational approach. The most favorable scheme of complexation for each type of the metal ion can be predicted. The theoretically predicted spectroscopic data of various forms of complexes, which are useful in the structural identification, have been described.

2. Computational details

2.1. Conformational study of (+)-catechin and its deprotonated species

The theoretical predictions provide more specific information on the OH groups at which each step of deprotonation preferably takes place based on the molecular thermodynamic quantities. The preferential deprotonation pathway of the neutral (+)-catechin conformer can be described as a series of four consecutive single-proton withdrawal processes, in which all substances involved are the most stable conformers of the respective species, i.e., the neutral ($CatH_5$), mono-anionic ($CatH_4^-$), di-anionic ($CatH_3^{2-}$), tri-anionic ($CatH_2^{3-}$) and tetra-anionic ($CatH^{4-}$) species. In finding the most stable conformation for each species, firstly, the molecular models of the possible conformers of $CatH_5$ were built. For each conformer built, the gas-phase molecular geometry optimization was carried out using the *Gaussian 03* program package [36]. The density functional theory (DFT) with the hybrid density functional B3LYP, i.e., Becke's three-parameter exchange functional [37] combined with the Lee–Yang–Parr correlation functional [38] with the 6-311++G(d,p) basis set was applied to all computational processes. For the basis set used herein, including a set of diffuse functions (++) to the light atoms such as hydrogen is an appropriate approach as far as the deprotonation reactions are much concerned. The conformers with successfully optimized

geometries were subsequently brought to the process of vibrational frequency computations, where the zero-point corrections for the electronic energies and the thermodynamic quantities were determined. Among the optimized conformers obtained, the most stable conformer was the one with the lowest electronic energy. On a trial basis, the first deprotonation was assigned separately to four OH groups (at C3′, C4′, C5 or C7) on the most stable $CatH_5$ conformer, giving four forms of $CatH_4^-$ with different deprotonated sites. The geometry optimization was then performed on each of these forms and only the most stable one was taken as the reactant for the further deprotonation. Similar to the preceding deprotonation, in the second deprotonation, a single proton was removed separately from the three remaining OH groups on the most stable form of $CatH_4^-$, hence producing three forms of $CatH_3^{2-}$. The geometries of these forms were fully optimized, and again only the most stable one was taken to the further deprotonation. By continuing the procedure of proton removal and geometry optimization, the most stable forms of $CatH_2^{3-}$ and $CatH^{4-}$ were finally obtained. The solvation effects on the molecular structures and energetics were examined by repeating the DFT geometry optimization under the integral-equation-formalism polarizable continuum model (IEFPCM) of solvation [39]. In the IEFPCM approach, the solute molecule was placed in a theoretical cavity surrounded by a polarizable dielectric continuum of water (the dielectric constant of 78.39). The cavity for solute molecule was created from a series of interconnecting spheres, each of which was centered at the atomic position of non-hydrogen element in the solute molecule; the radii of these spheres were defined according to the UAKS United Atom Topological Model [48] implemented in the *Gaussian 03* program package. By the IEFPCM(UAKS)/DFT/B3LYP/6-311++G(d,p) computations, the Gibbs energies of solvation could be determined. The values of such the thermodynamic energies were used in the theoretical determination of pK_a values for each (+)-catechin species, as described in the next section. In addition, the so-called natural bond orbital (NBO) analysis, which allowed the determination of primary interactions between particular bond orbitals, was performed on the most stable species using the *NBO 3.1* program integrated within *Gaussian 03*. Formerly, the NBO analysis was applied to explain the degrees of charge delocalization for the Cr(III) complex with quercetin, one of the most abundant flavonoids [40]. Such the analysis is useful in describing a number of electronic effects present in each stable species including electron delocalization, lone-pair electron donation and intramolecular hydrogen bonding, all of which have significant influence on the charge distribution and conformational stability.

2.2. Theoretical prediction of acid dissociation constants

Presenting the gas-phase acidity in the forms of the relative enthalpy of deprotonation reactions allows direct comparisons with the data obtained from the mass spectrometry and collision-induced dissociation (CID) experiment [17]. For the solvated-phase acidity, however, determination of the acid dissociation constants would be the more appropriate approach as the experimental data are available in the form of such the constants. The thermodynamic cycle in Scheme 1 illustrates how the deprotonation of a species $CatH_n^{n-5}$ in aqueous solution is related to the same reaction in gaseous state. The deprotonation of $CatH_n^{n-5}$ in aqueous solution follows the reaction path (e), for which the standard Gibbs energy ($\Delta G^*_{aq,depro}$) is related to the acid dissociation constant (K_a) of $CatH_n^{n-5}$ through the relation:

$$pK_a = -\log K_a = \frac{\Delta G^*_{aq,depro}}{2.303RT}, \quad (1)$$

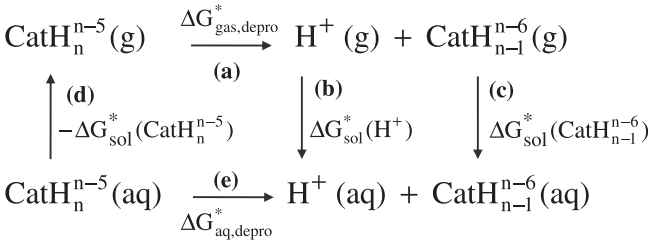

Scheme 1. Thermodynamic diagram used in the determination of the Gibbs free energies of deprotonation in aqueous solution for the species $CatH_n^{n-5}$ ($\Delta G^*_{aq,depro}$).

where the superscript (*) denotes the 1 M standard state of substances. Given the gas constant (R) and the temperature (T) are 1.986×10^{-3} kcal mol^{-1} K^{-1} and 298.15 K, respectively, Eq. (1) becomes:

$$pK_a = \frac{\Delta G^*_{aq,depro}\ /\text{kcal mol}^{-1}}{1.3644} \quad (2)$$

According to Scheme 1, $\Delta G^*_{aq,depro}$ can be written as:

$$\Delta G^*_{aq,depro} = \Delta G^*_{gas,depro} + \left[\Delta G^*_{sol}(H^+) + \Delta G^*_{sol}\left(CatH_{n-1}^{n-6}\right)\right] - \Delta G^*_{sol}\left(CatH_n^{n-5}\right) \quad (3a)$$

$$= \Delta G^*_{gas,depro} + \Delta\Delta G^*_{sol} \quad (3b)$$

where $\Delta G^*_{gas,depro}$ is the Gibbs energy of deprotonation for $CatH_n^{n-5}$ in gas phase. $\Delta G^*_{sol}(H^+)$, $\Delta G^*_{sol}\left(CatH_{n-1}^{n-6}\right)$ and $\Delta G^*_{sol}\left(CatH_n^{n-5}\right)$ are the Gibbs energies of solvation for H^+, $CatH_{n-1}^{n-6}$, and $CatH_n^{n-5}$, respectively. $\Delta\Delta G^*_{sol}$ is the net change in the Gibbs free energies of solvation upon deprotonation. The most recent theoretical–experimental value of −265.9 kcal mol^{-1} for $\Delta G^*_{sol}(H^+)$ was taken from the literature [41–44]. The Gibbs energy of deprotonation for $CatH_n^{n-5}$ in gas phase ($\Delta G^*_{gas,depro}$) can be calculated using following equation:

$$\Delta G^*_{gas,depro} = G^*_{gas}(H^+) + G^*_{gas}\left(CatH_{n-1}^{n-6}\right) - G^*_{gas}\left(CatH_n^{n-5}\right), \quad (4)$$

where $G^*_{gas}(H^+)$, $G^*_{gas}\left(CatH_{n-1}^{n-6}\right)$ and $G^*_{gas}\left(CatH_n^{n-5}\right)$ are the absolute Gibbs energies for H^+(g), $CatH_{n-1}^{n-6}$(g), and $CatH_n^{n-5}$(g), respectively. In the conventional gas-phase DFT calculations, the Gibbs energies in gas phase are determined at the 1 atm standard state. Conversion of the Gibbs energies at this standard state to the corresponding values at the 1 M standard state can be accomplished using following equation:

$$G^*_{gas} = G^o_{gas} + RT\ln(24.46). \quad (5)$$

Given the values $R = 1.987 \times 10^{-3}$ kcal mol^{-1} and $T = 298.15$ K, Eq. (5) becomes:

$$G^*_{gas} = G^o_{gas} + 1.89\ (\text{kcal mol}^{-1}). \quad (6)$$

Consequently, $\Delta G^*_{gas,depro}$ in Eq. (4) can be rewritten as:

$$\begin{aligned}\Delta G^*_{gas,depro} &= [G^o_{gas}(H^+) + 1.89] + [G^o_{gas}\left(CatH_{n-1}^{n-6}\right) + 1.89] \\ &\quad - [G^o_{gas}\left(CatH_n^{n-5}\right) + 1.89] \\ &= [G^o_{gas}(H^+) + G^o_{gas}\left(CatH_{n-1}^{n-6}\right) - G^o_{gas}\left(CatH_n^{n-5}\right)] \\ &\quad + 1.89 \\ &= \Delta G^o_{gas,depro} + 1.89. \end{aligned} \quad (7)$$

The values of $G^o_{gas}\left(CatH_{n-1}^{n-6}\right)$ and $G^o_{gas}\left(CatH_n^{n-5}\right)$ in Eq. (7) can be readily obtained from the DFT calculations of the gaseous species at 1 atm. The acceptable value of $G^o_{gas}(H^+)$ at 298.15 K is

−6.28 kcal mol^{-1} [45], derived from the Sackur–Tetrode equation for a monatomic ideal gas [46]. Such the value of $G^{o}_{gas}(H^{+})$ was applied in the calculations of the pK_a values for various substituted phenols [45] and carboxylic acids [47]. The pK_a values reported in this work were calculated using following equation:

$$pK_a = \frac{G^{o}_{gas}\left(CatH^{n-6}_{n-1}\right) - G^{o}_{gas}\left(CatH^{n-5}_{n}\right) + \Delta G^{*}_{sol}\left(CatH^{n-6}_{n-1}\right) - \Delta G^{*}_{sol}\left(CatH^{n-5}_{n}\right) - 270.29}{1.3644} \quad (8)$$

2.3. Structures of (+)-catechin-metal complexes

In the present study, (+)-catechin is treated as a bidentate ligand for the complexation with either zinc(II) or oxovanadium(IV). As displayed in Fig. 1b, upon complexation, the ligand uses two donor oxygen atoms at both C3′ and C4′ positions to chelate the metal ion, allowing five-membered chelate rings to be formed. Chelation by such the *ortho* catecholic oxygen atoms was described in the previous study on the complexation of (+)-catechin with copper and iron [48]. Using the other oxygen atoms at C3, C5, and C7 for chelation would also be inappropriate regarding long distances between them. To achieve satisfactory degrees of electron donation from donor atoms to metal ion, the (+)-catechin species with its hydroxyl protons at C3′ and C4′ being removed was chosen as the ligand in the complexation. The gas-phase optimized molecular structures of (+)-catechin-metal complexes were explored using the same DFT computational level as that used for the pure ligand. The metal-to-ligand (M:L) mole ratios at 1:1 and 1:2 were attempted in order to determine which ratio could lead to the most favorable complexation for each type of metal ion. The so-called time-dependent DFT (TD-DFT) single-point computations at the IEFPCM(UAKS)/TD-DFT/B3LYP/6-311++G(d,p) level were performed on the gas-phase optimized structures in the evaluation of the UV/visible absorption spectra for the complexes under hydration. Structural changes upon solvation of the gas-phase optimized geometries were assumed to have negligible effects on the UV/visible absorption, avoiding too expensive PCM computations for the large metal complexes. Previously, the TD-DFT methodologies were reported as being effective in describing the UV/visible electronic spectra of iron complexes of various flavonoids as well [49,50]. The *GaussSum 2.2.0* program [51] was used to generate the computational IR and UV/visible spectra.

3. Results and discussion

3.1. Conformational stability of (+)-catechin

As shown in Fig. 2, a series denoted as "series A" represents a group of the stable $CatH_5$ conformers, all of which are of successfully optimized geometries. The differences between the conformers in this series are mainly due to the variation of the hydroxyl proton configuration. The most stable conformer labeled as **5H-1** has the lowest electronic energy, whereas the electronic

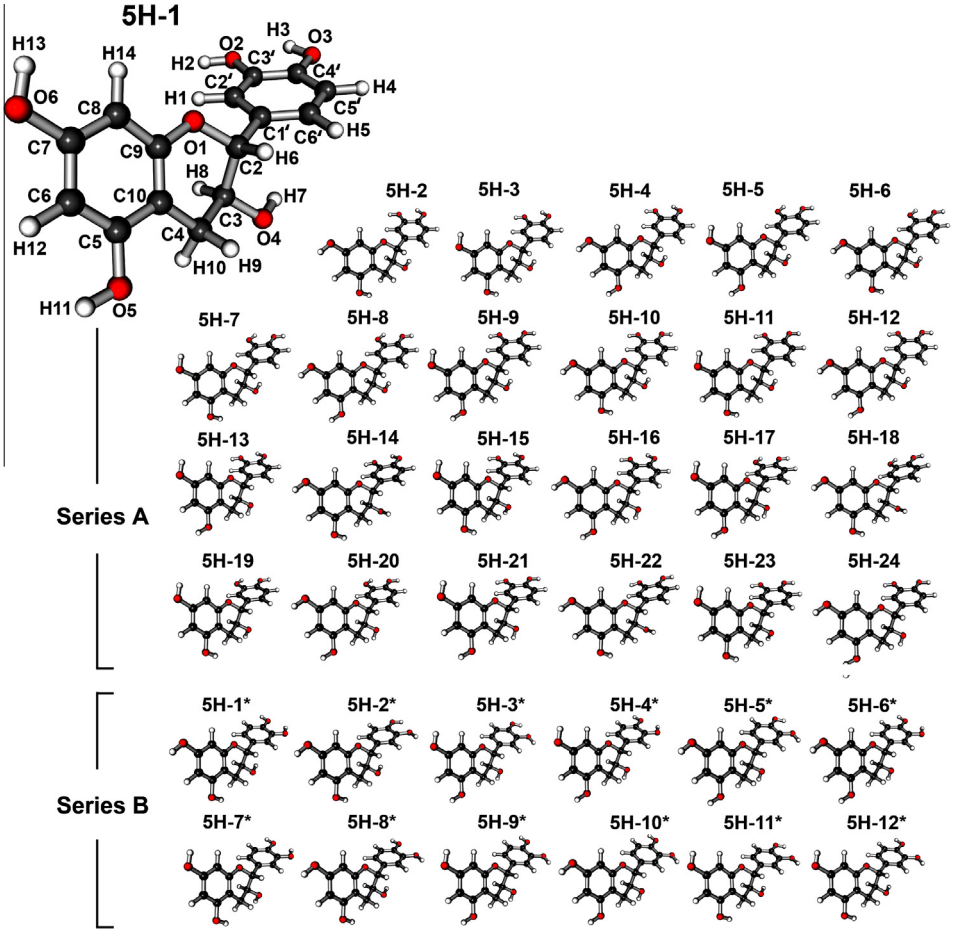

Fig. 2. Two series, denoted as series A and B, for the stable conformers of $CatH_5$. The major difference between the two series is the orientation of the ring B. For each series, the conformational stability decreases from left to right as well as from top to bottom. Atomic labeling as shown for the most stable conformer **5H-1** is applied to all (+)-catechin species in the present study.

energy for the least stable conformer (**5H-24**) is higher than that for **5H-1** by 154.64 kcal mol^{-1}. Clearly, for all stable conformers, the rings A and B are of the planar structure, implying considerable levels of electron delocalization on the two rings. This structural feature is missing for the ring C. The observation made on the first eight stable conformers of series A (**5H-1** to **5H-8**) suggests that the intramolecular hydrogen bonding within the proximity of two OH groups at C3′ and C4′ on the ring B is crucial in stabilizing the conformation. The O2–H3 hydrogen bond distance in **5H-1** is 2.153 Å.

The energy profile in Fig. 3a demonstrates how the single-point electronic energy of the conformer **5H-1** varies with the orientation of hydroxyl proton H7 at C3. This demonstration is not trivial as the real molecule in solution would possess certain degrees of flexibility, resulting in the structural fluctuations about the most stable form. The orientation of the ring B is left as it is in **5H-1** while the H7–O4 bond on the ring C is allowed to be rotated about the C3–O4 axis. The electronic energy is globally minimal at the H7–O4–C3–C2 dihedral angles of −59.9° and −59.9° + 360.0°, consistent with the unperturbed **5H-1** conformation. These two dihedral angles coincide with a very small dihedral angle H7–O4–C1′–C4′ (−2.9°), hence suggesting that the H7–O4 bond on the ring C and the C4′–O3 axis on the ring B lie almost in the same plane in order that the conformational energy can reach the minimum. The energy rises to the maxima when the dihedral angle H7–O4–C3–C2 is increased successively by about 90°. Besides the hydrogen bonding and the H7–O4 orientation, the orientation of the ring B plane has much influence on the conformational stability. In the most stable **5H-1** the dihedral angle C2′–C1′–C2–C3 is 80.5°, indicating that the rings B and C are almost perpendicular to each other (although the ring C is non-planar).

Now consider the case when the configuration of proton at C3 is stationary as is in the most stable conformation **5H-1** while the ring B plane is allowed to be rotated about the C1′–C2 bond. Such the rotation gives rise to the energy profile shown in Fig. 3b, where the change in the rotation angle is equivalent to the change in the dihedral angle O1–C2–C1′–C2′. Two global minima representing the unperturbed **5H-1** conformation are noticed at the O1–C2–C1′–C2′ dihedral angles of −40.6° and 319.4°. Interestingly, a local minimum of energy is observed at an intermediate O1–C2–C1′–C2′ dihedral angle of 124.4°. At this point, the plane of the ring B is rotated by 165° about the C1′–C2 bond from the initial orientation in **5H-1**, hence turning the OH group at C3′ (i.e., O2–H2) to the opposite side. This finding suggests that, apart from those in series A, another series of stable $CatH_5$ conformers may exist. Essentially, as shown in Fig. 2, twelve stable conformers have been found belonging to such the series, hereafter denoted as "series B". Similar to series A, the stabilization effect of hydrogen bonding on the ring B is still obvious in series B, especially in the first eight stable conformers (**5H-1***–**5H-8***). Table 1 summarizes the electronic energies, enthalpies, and Gibbs energies for all $CatH_5$ conformers depicted in Fig. 2. All energetic parameters are presented as the quantities relative to those of the most stable conformer **5H-1**. Excluding the most stable conformer **5H-1**, the conformers in series A show lower stability (i.e., higher electronic energies) than those in series B. Therefore, the conformational stability of the **5H-1** is uniquely high compared to the rest conformers in the same series.

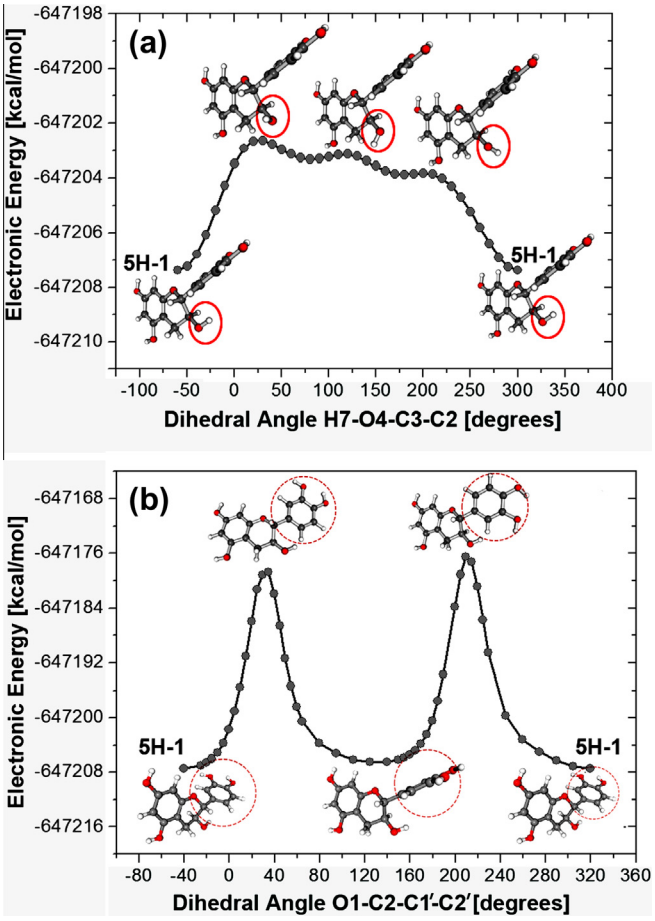

Fig. 3. Electronic energy profiles for $CatH_5$ plotted against (a) the dihedral angle H7–O4–C3–C2 and (b) the dihedral angle O1–C2–C1′–C2′. In both cases, the leftmost and the rightmost data points in the plots correspond to the unperturbed conformation for **5H-1**.

Table 1
Relative electronic energies (ΔE_{rel}), relative enthalpy (ΔH_{rel}) and relative Gibbs free energy (ΔG_{rel}) for the conformers of the neutral (+)-catechin ($CatH_5$) displayed in Fig. 2.

Conformer	Conformation series	ΔE_{rel} (kcal mol^{-1})	ΔH_{rel} (kcal mol^{-1})	ΔG_{rel} (kcal mol^{-1})
5H-1	A	0.0	0.0	0.0
5H-1*	B	1.2	1.3	1.0
5H-2*	B	1.3	1.4	1.2
5H-3*	B	2.1	2.3	1.8
5H-4*	B	2.4	2.5	2.0
5H-5*	B	2.8	3.1	2.1
5H-6*	B	3.1	3.3	2.0
5H-7*	B	3.6	4.0	2.7
5H-8*	B	5.3	5.4	5.2
5H-9*	B	6.2	6.4	5.9
5H-10*	B	6.9	7.2	6.6
5H-11*	B	19.2	19.1	19.4
5H-12*	B	23.2	23.1	23.6
5H-2	A	147.0	146.9	147.1
5H-3	A	147.3	147.3	147.4
5H-4	A	147.5	147.4	147.6
5H-5	A	147.6	147.5	147.6
5H-6	A	147.7	147.7	147.8
5H-7	A	147.9	147.9	148.0
5H-8	A	147.9	147.9	148.1
5H-9	A	148.7	148.8	148.5
5H-10	A	148.9	149.0	148.8
5H-11	A	149.4	149.6	149.1
5H-12	A	149.7	149.8	149.5
5H-13	A	149.9	149.7	149.9
5H-14	A	150.3	150.5	149.9
5H-15	A	150.4	150.5	150.2
5H-16	A	150.8	150.7	150.9
5H-17	A	150.8	151.0	150.6
5H-18	A	151.5	151.5	151.5
5H-19	A	151.6	151.6	151.7
5H-20	A	151.7	151.7	151.8
5H-21	A	152.8	152.9	152.6
5H-22	A	153.6	153.7	153.3
5H-23	A	154.0	153.8	154.1
5H-24	A	154.6	154.7	154.5

3.2. Donor–acceptor bond orbital interactions and charge density distribution

The detailed electronic behaviors of the neutral (+)-catechin and its deprotonated species are crucial in understanding the molecular stability, charge density distribution and intramolecular interactions. The important results as obtained from the NBO analysis and the electrostatic potential mapping for the most stable forms of various (+)-catechin species: $CatH_5$ [**5H-1**], $CatH_4^-$ [**4H(3′)**], $CatH_3^{2-}$ [**3H(3′5)**], $CatH_2^{3-}$ [**2H(3′57)**] and $CatH^{4-}$ [**1H(3′574′)**] are described as follows:

(a) **5H-1**. The bonding (BD)–antibonding (BD*) orbital interactions between the vicinal carbon–carbon bonds on the rings A and B of **5H-1** are of high energies up to 25.7 and 20.1 kcal mol^{-1}, respectively (see Table 2), indicating large extent of electron delocalization over the individual rings. The ring A shows greater extent of electron delocalization than the ring B and this is also true in the cases of **2H(3′57)** and **1H(3′574′)**. The electrostatic potential (ESP) maps for the most stable conformers: **5H-1**, **3H(3′5)**, **2H(3′57)** and **1H(3′574′)** are illustrated in Fig. 4. Based on the molecular orientation of **5H-1** as shown in Fig. 4, high densities of negative charges are observed over the upper part of the two interconnected rings A and C, most particularly in the region near C9. According to the BD−BD* interaction energies listed in Table 2, the displacement of pi-electrons over the ring A essentially favors the following directions: (C5–C6) → (C7–C8) and (C7–C8) → (C9–C10). The electrons therefore show tendency of moving to the upper half of the ring A (in reference to Fig. 4). Also, donation of the lone-pair (LP) electrons from either O1 or O6 to the ring A is important due to high energies for the interactions LP(O1)–BD*(C9–C10) (25.8 kcal mol^{-1}) and LP(O6)–

Table 2
Selected donor–acceptor natural bond orbital interactions with the respective interaction energies.

Orbital interaction		Interaction energy (kcal/mol)				
Donor	Acceptor	**5H-1**	**4H(3′)**	**3H(3′5)**	**2H(3′57)**	**1H(3′574′)**
BD(C5–C6)	BD*(C7–C8)	25.7	25.5		30.5	30.0
BD(C7–C8)	BD*(C5–C6)	12.5	12.2	–	8.4	8.3
BD(C7–C8)	BD*(C9–C10)	24.6	23.2	–	39.2	36.3
BD(C9–C10)	BD*(C7–C8)	13.5	14.0	–	8.3	8.6
BD(C9–C10)	BD*(C5–C6)	25.6	29.4	–	19.4	21.4
BD(C5–C6)	BD*(C9–C10)	13.0	12.0	–	9.2	8.9
BD(C1′–C6′)	BD*(C2′–C3′)	19.1	12.2	–	13.0	12.0
BD(C2′–C3′)	BD*(C1′–C6′)	18.9	28.0	–	27.6	23.8
BD(C4′–C5′)	BD*(C1′–C6′)	20.1	17.1	15.6	14.8	22.7
BD(C1′–C6′)	BD*(C4′–C5′)	18.8	15.7	17.3	18.7	12.7
BD(C4′–C5′)	BD*(C2′–C3′)	20.0	13.9	–	13.9	10.8
BD(C2′–C3′)	BD*(C4′–C5′)	18.3	16.1	–	18.4	11.8
BD(C3′–C4′)	BD*(C4′–C5′)	–	–	4.1	4.3	1.4
BD(C2′–C3′)	BD*(C1′–C2′)	–	–	3.4	3.3	3.4
BD(C4′–C5′)	BD*(C5′–C6′)	–	–	3.2	3.1	3.1
BD(C8–C9)	BD*(C9–C10)	–	–	5.1	5.7	5.0
BD(C7–C8)	BD*(C6–C7)	–	–	4.9	1.9	2.1
BD(C5–C6)	BD*(C6–C7)	–	–	2.8	2.0	2.0
BD(C7–C8)	BD*(C8–C9)	–	–	3.0	2.7	2.7
LP(O1)	BD*(C9–C10)	25.8	32.1	23.8	18.1	21.2
LP(O1)	BD*(C2–C3)	3.1	2.6	3.4	4.1	3.3
LP(O2)	BD*(C2′–C3′)	23.9	72.6	13.6	60.4	69.6
LP(O2)	BD*(C3′–C4′)	0.8	13.2	12.2	11.5	16.4
LP(O2)	BD*(O3–H3)	0.8	10.9	12.0	13.4	–
LP(O3)	BD*(C4′–C5′)	27.5	29.9	27.6	25.9	11.4
LP(O4)	BD*(C2–C3)	6.4	4.6	3.7	3.1	3.2
LP(O4)	BD*(O2–H2)	16.6	–	–	–	–
LP(O4)	BD*(O5–H11)	–	17.5	–	–	–
LP(O5)	BD*(C5–C6)	27.9	26.6	14.8	69.8	65.2
LP(O5)	BD*(C5–C10)	–	–	15.3	13.7	13.1
LP(O6)	BD*(C7–C8)	28.1	25.9	4.6	69.5	12.8
LP(O6)	BD*(C6–C7)	–	–	21.5	12.5	11.7
BD(O3–H3)	BD*(C4′–C5′)	4.6	6.2	6.2	6.3	–
BD(C4′–C5′)	BD*(O3–H3)	1.5	1.1	1.0	1.0	–
BD(O3–H3)	BD*(C3′–C4′)	0.6	0.9	0.9	0.9	–
BD(O4–H7)	BD*(O2–H2)	4.9	–	–	–	–
BD(C3–O4)	BD*(O2–H2)	2.7	–	–	–	–
BD(C7–O6)	BD*(C6–C7)	0.6	0.6	0.5	1.8	1.6
BD(C7–O6)	BD*(C7–C8)	0.9	0.8	–	1.4	1.4
BD(C5–O5)	BD*(C5–C6)	0.9	0.8	1.7	1.9	1.7
BD(C5–O5)	BD*(C9–C10)	1.7	1.7	4.0	1.5	1.4
BD(C5–O5)	BD*(C5–C10)	0.9	0.9	1.8	1.4	1.4
BD(C3′–O2)	BD*(C2′–C3′)	1.1	2.7	2.5	2.4	1.8
BD(C3′–O2)	BD*(C4′–C5′)	1.6	1.6	4.7	1.8	0.8
BD(C3′–O2)	BD*(C1′–C2′)	1.2	1.1	1.1	1.1	1.6
BD(C3′–O2)	BD*(C3′–C4′)	–	1.0	1.0	0.9	0.8
BD(C4′–O3)	BD*(C2′–C3′)	1.4	1.3	1.3	1.4	0.8
BD(C4′–O3)	BD*(C4′–C5′)	1.0	1.2	1.1	1.0	1.8
BD(C4′–O3)	BD*(C5′–C6′)	1.3	1.4	1.4	1.4	1.6
BD(C3–O4)	BD*(C2–O1)	1.6	1.7	1.5	1.4	1.4
BD(C3–O4)	BD*(C4–C10)	1.2	1.3	1.1	1.0	1.0

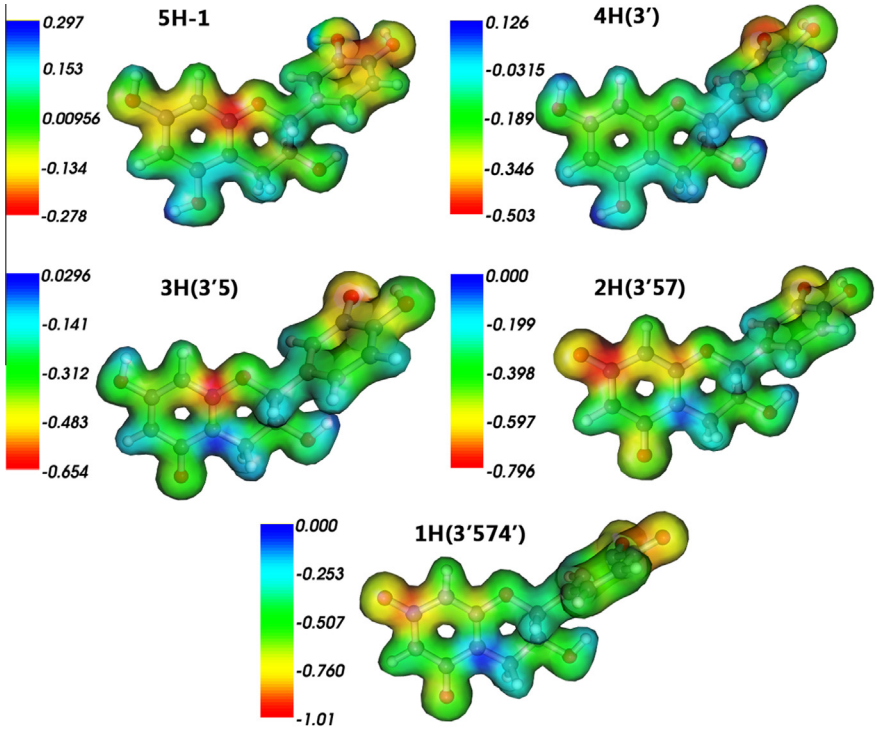

Fig. 4. Electrostatic potential maps, generated with isosurface value of 0.010 e Å^{-3}, for the most stable conformers of $CatH_5$ [**5H-1**], $CatH_4^-$ [**4H(3′)**], $CatH_3^{2-}$ [**3H(3′5)**], $CatH_2^{3-}$ [**2H(3′57)**], and $CatH^{4-}$ [**1H(3′574′)**].

BD*(C7–C8) (25.8 kcal mol^{-1}). Both LP orbital interactions induce high negative charge densities over the C7–C8–C9 segment, whereas the donation of LP(O1) electrons to BD*(C2–C3) on the right hand side of the ring C is not as attainable as the donation to BD*(C9–C10) on the left hand side of the same ring (with reference to Fig. 4). The ESP map of **5H-1** also reveals that the positive charges are localized predominantly on either H3 (the ring B) or H11 (the ring A), implying both H3 and H11 show high tendency of being released as protons. For the ring B with the *ortho*-oxygen atoms, the degree of electron displacement is comparable in either clockwise or counterclockwise directions (with reference to Fig. 4) along the interconnected carbon–carbon bonds. However, the electron donation from both LP(O2) and LP(O3) to the BD* orbitals on the ring B corresponds to the high interaction energies up to 27.5 kcal mol^{-1}, leading to the accumulation of negative charge densities over the C3′–C4′–C5′ segment. Basically, the electron delocalization on both rings is further enhanced by the donation of electrons from the LP orbitals on oxygen atoms. For instance, the LP orbital on O6, with an almost pure p character (s 0.00%, p 99.94%, d 0.06%) and a occupancy of 1.88, interacts strongly with the BD*(C7–C8) orbital [i.e., 0.7566 p(C7)–0.6539 p(C8)], yielding high interaction energy at 28.1 kcal mol^{-1}. The LP(O5)–BD*(C5–C6) and LP(O3)–BD*(C4′–C5′) interactions are at similarly high levels. The LP(O2) electron donation to BD*(C2′–C3′) shows quite lower interaction energy at 23.9 kcal mol^{-1}; however this value is still sufficiently high. In contrast, the LP(O4) electrons interact weakly with the BD* orbitals on the ring C, but much more strongly with BD*(O4–H7). This effect leads to the decrease in positive charges on H7. In addition, the LP(O4) orbital surprisingly interacts with the BD*(O2–H2) orbital on the remote ring B, yielding significant interaction energy at 16.6 kcal mol^{-1}. Possibly, this interaction well stabilizes the configuration of H2 as observed in **5H-1**. The LP(O2)–BD*(O3–H3) orbital interaction principally accounts for the hydrogen bonding between O2 and H3; such the interaction corresponds to the low interaction energy at 0.8 kcal mol^{-1}, which is moderately significant in terms of hydrogen bonding.

(b) **4H(3′)**. In the ESP map for **4H(3′)** shown in Fig. 4, the bottom parts of the rings A and C exhibit high positive charge densities while the negative charges are located mostly on the upper part similar to **5H-1**. The negative charges on the upper part, however, appear more uniformly distributed in this case, possibly due to the changes in two types of orbital interactions. Firstly, the marked increase in the BD(C9–C10)–BD*(C5–C6) interaction energy assists the transfer of negative charges to the lower part of the ring A. Secondly, the slight decrease in the energies of two LP orbital interactions: LP(O6)–BD*(C7–C8) and LP(O5)–BD*(C5–C6) leads to the lowering of negative charge densities over the upper half of the ring A. The negative charges are located most intensely over the C3′–O2 segment followed by the neighboring O3. The donation of LP(O2) and LP(O3) electrons to the BD* orbitals on the ring B is more feasible as evident from the increase in the interaction energies: LP(O2)–BD*(C2′–C3′), LP(O2)–BD*(C3′–C4′), and LP(O3)–BD*(C4′–C5′); however the BD–BD* orbital interactions on the ring B are weakened compared to **5H-1**, with the exception only for BD(C2′–C3′)–BD*(C1′–C6′). These effects not only lower the extent of electron delocalization over the ring B but also produce the high densities of negative charges near C3′ and C4′, in agreement with the ESP observations on the ring B in **4H(3′)**. The hydrogen bonding between the highly negatively charged O2 and the vicinal H3 is immensely strengthened as the LP(O2)–BD*(O3–H3) interaction energy is increased dramatically to 10.9 kcal mol^{-1}, hence disfavoring the removal of H3 as a proton.

(c) **3H(3′5)**. The most notable behavior for the orbital interactions in **3H(3′5)** is the vanishing of vicinal BD–BD* orbital interactions on the ring A, induced by the loss of H11 from O5. Although the adjacent BD–BD* orbital interactions on the ring A, for example, BD(C8–C9)–BD*(C9–C10), BD(C7–C8)–BD*(C6–C7) or BD(C5–C6)–BD*(C6–C7) are present, they are rather weak, exhibiting low interaction energies ranging from 3.0 to 5.1 kcal mol^{-1}. This result indicates the decrease in the level of electron delocalization over the ring A. The negative charge densities are intensely localized in the region near C9 as seen in Fig. 4, most likely due to the donation of LP(O1) to BD*(C9–C10) (the interaction energy = 23.8 kcal mol^{-1}). Overall, the LP(O2) orbital interactions (12.0–13.6 kcal mol^{-1}) are weaker than the LP(O5) orbital interactions (14.8–15.3 kcal mol^{-1}). This implies the negative charge densities are more localized around the donor O2 than O5, in accordance with the ESP observations. The behavior of the LP(O3) orbital interaction in **3H(3′5)** is not much different from that in **5H-1**. The increase in the LP(O2)–BD*(O3–H3) interaction energy is observed, indicating the hydrogen bonding between O2 and H3 is further reinforced.

(d) **2H(3′57)**. The BD–BD* orbital interactions between the vicinal carbon–carbon bonds on the ring A are restored as a consequence of the H13 removal from O6. The greater BD(C5–C6)–BD*(C7–C8) and BD(C7–C8)–BD*(C9–C10) interactions suggest that the negative charges are localized more intensely along the C7–C8–C9 segment, in agreement with the ESP map. The remarkably high densities of negative charges observed near C7 are attributed to the combination of two types of strong interactions: BD(C5–C6)–BD*(C7–C8) (30.5 kcal mol^{-1}) and LP(O6)–BD*(C7–C8) (69.5 kcal mol^{-1}). The LP(O5) and LP(O2) orbitals show strong preference of electron donation to BD*(C5–C6) orbital (69.8 kcal mol^{-1}) and BD*(C2′–C3′) orbital (60.4 kcal mol^{-1}), respectively, reflecting the necessity of the lone-pair electron donation to the rings in the stabilization of negative charges produced upon deprotonation. The energy of the LP(O2)–BD*(O3–H3) interaction in **2H(3′57)** rises by 12% from the value in **3H(3′5)**, indicating the more enhanced hydrogen bonding in **2H(3′57)**.

(e) **1H(3′574′)**. The ESP map in Fig. 4 reveals high negative charge densities expanding almost the entire molecule of **1H(3′574′)**. The lowest densities of negative charges are observed on the ring C where the electron delocalization is not favorable. Similar to **2H(3′57)**, no positively charged regions are noticed. Furthermore, the region near C10 exhibits the charge densities close to zero as the donation of LP(O5) electrons to BD*(C5–C10) is not much feasible compared to the same electron donation to BD*(C5–C6). The behavior of BD–BD* orbital interactions on the ring A for **1H(3′574′)** is similar to that for **2H(3′57)** regarding the relevant interaction energies listed in Table 2. The overall LP(O2) electron donation to the ring B is much more enhanced regarding the strengthened interactions LP(O2)–BD*(C2′–C3′) (69.6 kcal mol^{-1}) and LP(O2)–BD*(C3′–C4′) (16.4 kcal mol^{-1}). The enhancement of the LP(O2)–BD*(C3′–C4′) interaction is however attained at the cost of the weakening of the neighboring LP(O3)–BD*(C4′–C5′) interaction.

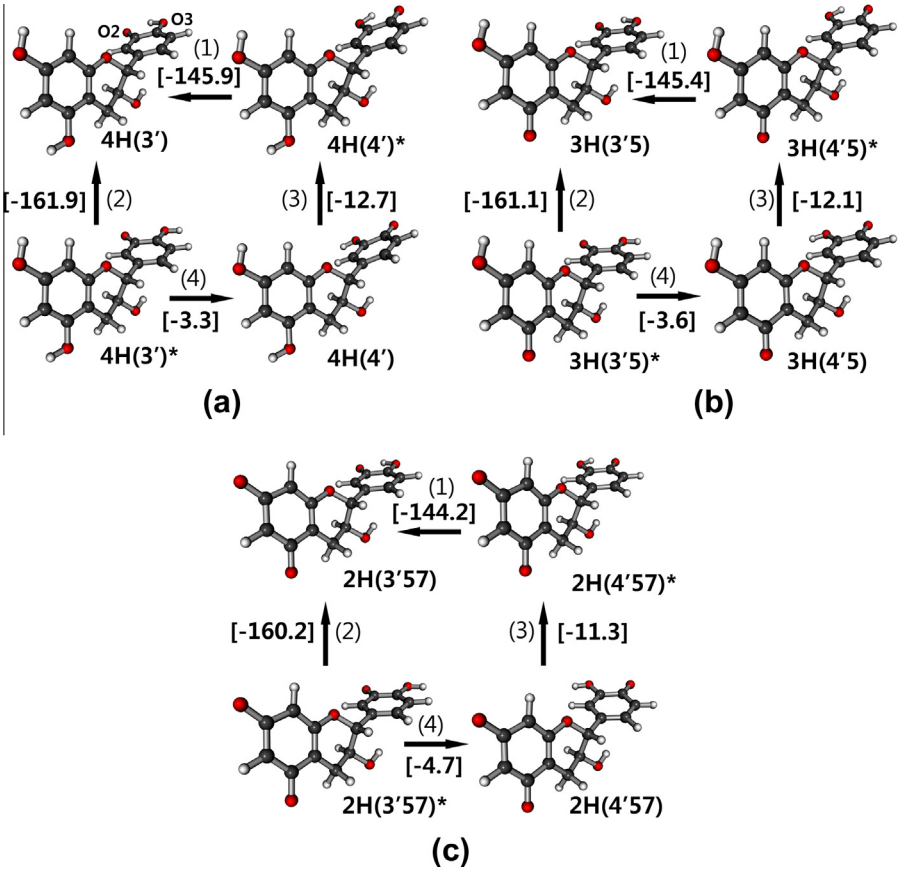

Fig. 5. Schematic representation of the proton transfer between two ortho-oxygen atoms, i.e., O2 and O3 [paths (1) and (4)] and the relevant reorientation of the hydroxyl protons [paths (2) and (3)] in (a) $CatH_4^-$, (b) $CatH_3^{2-}$ and (c) $CatH_2^{3-}$. The values in square brackets are the reaction Gibbs energies in kcal mol^{-1}.

3.3. Extent of proton transfer between ortho-catecholic oxygen atoms

Given the average O2–O3 and O3–H3 distances in the three deprotonated species: $CatH_4^-$ [**4H(3′)**], $CatH_3^{2-}$ [**3H(3′5)**], $CatH_2^{3-}$ [**2H(3′57)**] at 2.6 Å and 1.0 Å, respectively, the proton transfer between O3 and O2 in these three species in solution could possibly take place. In Fig. 5, various proton transfer reactions for $CatH_4^-$, $CatH_3^{2-}$, and $CatH_2^{3-}$ are displayed along with the Gibbs energies involved. All structures depicted are of the optimized geometries and all reaction paths are spontaneous with the negative values of the Gibbs energies. The paths (1a), (1b) and (1c) shown in Fig. 5 are the direct proton exchange reactions. The paths (2a)–(2c) and (3a)–(3c) represent the rotation of the O–H bond about the C–O axis, whereas (4a)–(4c) can be regarded as the proton transfer reactions concerted with the hydroxyl proton reorientation. Obviously, any paths that lead to the most stable conformers [**4H(3′)**, **3H(3′5)** or **2H(3′57)**] correspond to the large absolute values of the reaction Gibbs energies at 144–146 or 160–162 kcal mol^{-1}, suggesting high preference of the transformation to the most stable conformation. For the reaction paths (1), (2) and (3), the absolute value of the Gibbs energy decreases slightly with decreasing number of the hydroxyl protons in the molecule; therefore these reactions become less favorable upon deprotonation. In contrast, the proton transfer reactions (4a), (4b) and (4c) follow different trend as the reaction is increasingly favorable with more hydroxyl protons being withdrawn from the molecule; however, the absolute values of the Gibbs energies are small (3–5 kcal mol^{-1}) due to the absence of intramolecular hydrogen bonding.

3.4. Frontier molecular orbitals for (+)-catechin species

The energy levels of two frontier molecular orbitals (FMOs), namely, the highest occupied molecular orbital (HOMO) and the lowest unoccupied molecular orbital (LUMO) derived at the B3LYP/6-311++G(d,p) level are displayed in Table 3 for all (+)-catechin species. The HOMO–LUMO gaps are in the decreasing order: **5H-1** > **3H(3′5)** > **4H(3′)** > **1H(3′574′)** > **2H(3′57)**. Based on the Koopman theorem, the chemical hardness (η) is proportional to the HOMO–LUMO gap: $\eta = \frac{E_{LUMO}-E_{HOMO}}{2}$ [52,53]. The deprotonated species **1H(3′574′)** and **2H(3′57)** can be regarded as highly polarizable or "soft" anionic species due to their small HOMO–LUMO gaps. These two soft anionic species are predicted to be more chemically reactive than the others for unimolecular reactions such as isomerization or decomposition. On the other hand, the neutral species **5H-1** shows the widest HOMO–LUMO gap at 5.36 eV. The electronic transition from its HOMO to LUMO requires high excitation energy, implying that the deprotonation could introduce the red-shift to the UV/visible spectral bands of (+)-catechin. In several cases, besides the HOMO–LUMO transition, the other MO transitions could have greater contributions to the observed spectral bands. The FMO energy levels have been found to fit well with the linear relations: E_{HOMO} (eV) = 3.44x − 5.40 (R^2 = 0.985) and E_{LUMO} (eV) = 2.26x − 0.77 (R^2 = 0.996), where x is the number of proton being withdrawn from the neutral (+)-catechin (x = 0, 1, 2, 3 and 4). Upon deprotonation, E_{HOMO} thus increases at higher rate than E_{LUMO}. This implies that the chemical instability is laid upon the deprotonated species. With the lowest lying LUMO energy, **5H-1** is predicted to be the best Lewis acid (electron-pair acceptor) compared to the other species whereas the deprotonated species with the elevated HOMO energy levels have higher tendency to act as the Lewis base (electron donor). The homolytic O–H bond dissociation in any $CatH_n^{n-5}$ species produces the phenoxyl radical and the hydrogen radical, following as $CatH_n^{n-5}(g) \rightarrow {\bullet}CatH_{n-1}^{n-5}(g) + {\bullet}H(g)$. The bond dissociation enthalpy (BDE) involved in such the reaction can be determined with the relation: $BDE = H^o({\bullet}H) + H^o({\bullet}CatH_{n-1}^{n-5}) - H^o(CatH_n^{n-5})$.As shown in Table 3, the BDE values for various (+)-catechin species in gas phase lie in a range of 65–75 kcal mol^{-1}, which is not so broad as all enthalpy values similarly correspond to the dissociation of the same type of bond. Nevertheless, deprotonation causes the decrease in the BDE value, indicating that the deprotonated species tends to break into free radicals more easily than the protonated species; the same tendency could be expected for the species in solution. Therefore, at high pH values, formation of phenoxyl and hydrogen radicals should be facilitated. As shown in Table 3, the decrease in the HOMO–LUMO gap is noticed for the phenoxyl radicals ${\bullet}CatH_{n-1}^{n-5}$, similar to the observations on the phenoxylate species. Both HOMO and LUMO energies for the phenoxyl radicals lie lower than those for their respective phenoxylates. For example, E_{HOMO} and E_{LUMO} for the phenoxylate $CatH_4^{-1}$ are −1.08 eV and 1.33 eV, respectively, whereas E_{HOMO} and E_{LUMO} for the phenoxyl radical ${\bullet}CatH_4$ are −6.23 eV and −1.05 eV, respectively. The lowering in the LUMO level suggests that the phenoxyl radicals are more electrophilic than their respective phenoxylate species.

Table 3
Electronic and energetic parameters determined for various (+)-catechin species.

(+)-Catechin species/conformer	E_{HOMO} (eV)	E_{LUMO} (eV)	$\Delta E_{LUMO-HOMO}$ (eV)	η[a]	BDE[b] (kcal mol^{-1})
$CatH_5$/**5H-1**	−6.10	−0.74	5.36	2.68	75.2
$CatH_4^{-1}$/**4H(3′)**	−1.08	1.33	2.41	1.21	73.5
$CatH_3^{-2}$/**3H(3′5)**	1.33	4.09	2.76	1.38	70.2
$CatH_2^{-3}$/**2H(3′57)**	5.41	5.75	0.34	0.17	65.4
$CatH^{-4}$/**1H(3′574′)**	7.86	8.36	0.50	0.25	–
Free radical species					
${\bullet}CatH_4$	−6.23	−1.05	5.18	2.59	
${\bullet}CatH_3^{-1}$	−2.47	1.72	4.19	2.10	
${\bullet}CatH_2^{-2}$	0.92	3.92	3.00	1.50	
${\bullet}CatH^{-3}$	4.40	6.26	1.86	0.93	

[a] Chemical hardness: η ($E_{LUMO} - E_{HOMO}$)/2.
[b] Homolytic O–H bond dissociation enthalpy (BDE): BDE $H^o({\bullet}H) + H^o({\bullet}CatH_{n-1}^{n-5}) - H^o(CatH_n^{n-5})$, for the $CatH_n^{n-5}$ species.

3.5. Theoretically preferential deprotonation pathway of (+)-catechin

The preferential deprotonation pathway of (+)-catechin in aqueous solution is schematically displayed in Fig. 6. In terms of molecular structure, the most stable forms of $CatH_5$ [**5H-1**], $CatH_4^-$ [**4H(3′)**], $CatH_3^{2-}$ [**3H(3′5)**], $CatH_2^{3-}$ [**2H(3′57)**] and $CatH^{4-}$ [**1H(3′574′)**] exhibit somewhat similar geometries regardless of the number of the hydroxyl protons attached. As depicted in Fig. 6, the most stable form of $CatH_4^-$, **4H(3′)**, is the one with the hydroxyl proton at C3′ being removed. The OH group at C3′ is therefore the most acidic site on the molecule, corresponding to $pK_{a(1)}$ = 9.3, lying in a typical pK_a range for phenols. As shown by the structure of **4H(3′)** in Fig. 6, after the first deprotonation, the hydroxyl proton at C4′ remains pointed to the oxide group at C3′, indicative of significant electrostatic interaction between this proton and the negatively charged oxygen. This in turn prevents the hydroxyl proton at C4′ from being withdrawn, causing the further deprotonation to take place on the ring A instead. Consistently, the second most acidic site of (+)-catechin is the OH group at C5 on the ring A, with $pK_{a(2)}$ = 10.6, being larger than the preceding $pK_{a(1)}$ by 12%. The OH group at C7 is the third most acidic site, with $pK_{a(3)}$ = 13.4. The OH group at C4′ is responsible for the fourth deprotonation, corresponding to the highest $pK_{a(4)}$ value at 16.0. The difference in the pK_a values between the least and the most acidic OH groups is as large as 7. The extent of acid dissociation for the least acidic OH group at C4′ is very low, being $\sim 10^7$ times lower than that for the most acidic OH group at C3′. Based

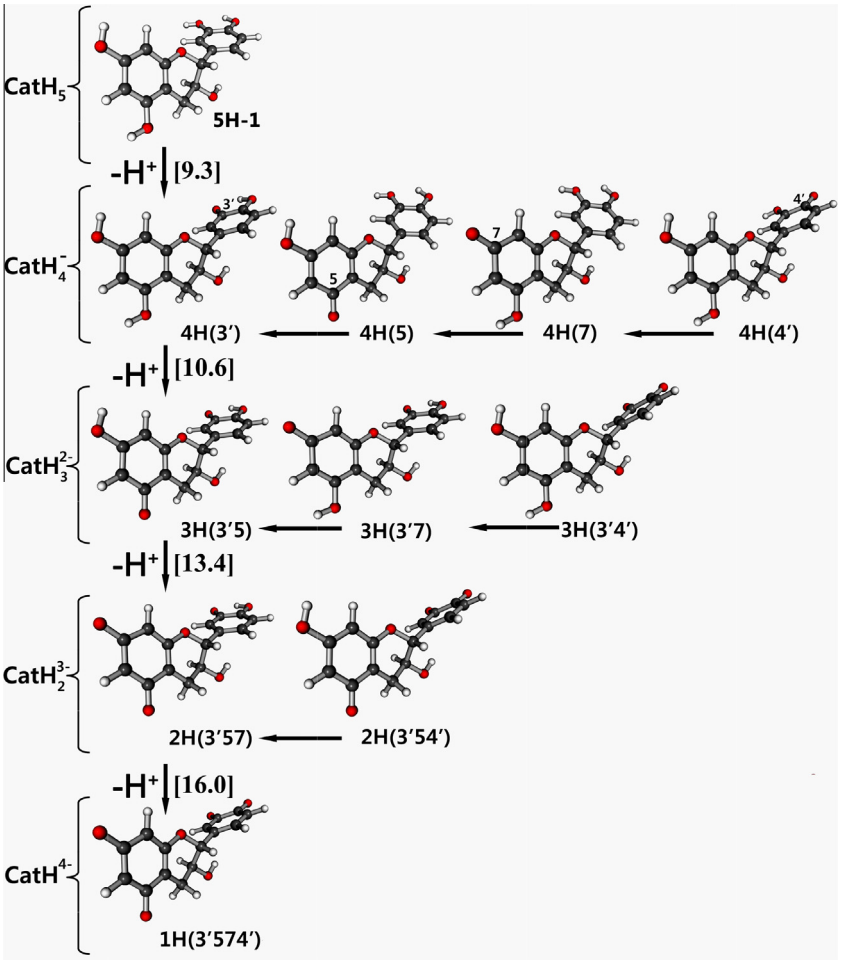

Fig. 6. Various stable isomers possibly formed upon deprotonation of the most stable conformer of $CatH_5$ (**5H-1**). For the deprotonated species shown in each row, the thermodynamic stability increases from right to left (as indicated by the horizontal arrows). The serial numbers in parentheses for the isomer labels represent the sites where the deprotonation takes place in sequence. The most favorable deprotonation pathway is depicted vertically, with the predicted pK_a values given in the square brackets.

Table 4
The pK_a values for the hydroxyl groups on (+)-catechin predicted in the present work shown together with the values from the previous works.

pK_a	Present work	Previous work					
		Slabbert [12]	Kennedy et al. [13]	Herrero-Martinez et al. [14]		Cren-Olivé et al. [15,16]	Muzolf et al. [7]
p$K_{a(1)}$	9.3 (C3′/B)	8.97 (B)	8.64 ± 0.01 (B)	9.11 [a] (C3′/B)	8.85 [b] (C3′)	9.02 (C3′/B)	8.58 [c]
p$K_{a(2)}$	10.6 (C5/A)	9.26 (A)	9.41 ± 0.02 (A)	10.39 [a] (C5/A)	10.23 [b] (C5,C7)	9.12 (C4′/B)	
p$K_{a(3)}$	13.4 (C7/A)	11.18 (A)	11.26 ± 0.06 (B)	11.94 [a] (C7/A)	12.16 [b] (C7, C4′)	9.43 (C5/A)	
p$K_{a(4)}$	16.0 (C4′/B)	13.25 (B)	13.26 ± 0.05 (A)			9.58 (C7/A)	

[a] Based on the structure–reactivity simulation using the SPARC program.
[b] Derived from the capillary electrophoretic data.
[c] Predicted with the QSAR approach.

on the local charges determined from the atomic polar tensor charge distribution, ionization of the secondary alcohol functional group at C3 into the oxide has been predicted to localize the charge of the amount −0.8 on the O4 oxygen atom. Since the ring C shows no degrees of electron delocalization, localization of negative charge on the oxygen atom at C3 is therefore less favorable than the case where the same oxygen atom is bound to the positively charged hydrogen. This renders the oxygen atom at C3 into the non-ionizable one compared to those at the other positions. In summary, the computed pK_a values for all OH groups in (+)-catechin follow as: p$K_{a(1)}$ (9.3) < p$K_{a(2)}$ (10.6) < p$K_{a(3)}$ (13.4) < p$K_{a(4)}$ (16.0). Therefore, acidity of the OH groups on (+)-catechin decreases in the order: C3′-OH (ring B) > C5-OH (ring A) > C7-OH (ring A) > C4′-OH (ring B). The following linear relationship has been found for the computed pK_a values of all (+)-catechin species: pK_a = 2.29x + 6.60 (R^2 = 0.978), where x is the total number of hydroxyl protons being removed from the neutral species. As shown in Table 4, compared to the experimental values from several previous works, the theoretical predictions made in the present study seem to overestimate the pK_a values for (+)-catechin. The smallest pK_a value at 9.3 obtained for the C3′-OH group in this work is in excellent agreement with the experimental values, within 0.7 pK_a units of error. The larger discrepancies observed for the higher pK_a values might be due to the fact that the PCM continuum solvation approach could not well predict the Gibbs energies of solvation for the charged species [44]. Barrone and

Cossi suggested that more solute charge could escape from the cavity for ionic solutes than for neutral solutes due to the exponential decay of electronic tails [54]. In addition, the most appropriate theoretical–experimental value of the Gibbs energy of solvation of $H^+(g)$ is currently on argument [44]. To match the experimental values better, a multiplying factor of ~0.9 was required for scaling our predicted pK_a values, hence yielding the approximate relationship: pK_a (experiment) ≈ 0.9 pK_a (prediction), with the exception of the data presented by Cren-Olivé et al. [15]. By this scaling approximation, the predicted pK_a values, except the smallest one, would in general be improved. Allowing for the fact that the acid dissociation constants determined from the real chemical systems depend on various factors (e.g., ionic strength, solvents, temperature, or impurity), the predicted pK_a values in this work are fairly reasonable. Also, it is worth pointing that the actual microscopic deprotonation phenomena at a given pH value could occur at the individual OH groups simultaneously in a competitive manner as suggested in the previous works [14,15]. Reproducing the composite pK_a values detected experimentally from such the weakly acidic compound as (+)-catechin would not be easily accomplished with the idealized, successive deprotonation treatment attempted in this work. Theoretical study on the parallel deprotonation pathways could be necessary in establishing more realistic models, but this would be complicated for such the tetraprotic compound. Otherwise, the DFT-based molecular dynamic simulation [55,56] might be used as an alternative method to accurately determine the pK_a values. However, in the present study, the explicit DFT computational approach associated with the IEFPCM solvation model was expected to afford a precise molecular picture of the primary deprotonation pathway in aqueous solution. The ring sequence of the preferential deprotonation: B–A–A–B agrees well with the original work by Slabbert [12] and the more recent work by Herrero-Martinez et al. [14]. The former DFT computations, combined with the external approximation such as qualitative structure-activity relationship (QSAR) obtained from a series of catechin-related compounds, was applied to estimate the p$K_{a(1)}$ value for (+)-catechin [7]. The bond dissociation energies used therein resulted from the single-point energy calculations rather than the proper geometry optimizations in order to save the computing time. Neither zero-point energy corrections, nor thermal contributions, nor solvation effects were taken into account as well. On the other hand, the previous study by Martins et al. [17] reported the importance of including the zero-point energy corrections in the gas-phase acidity calculations for several flavonoids including (+)-catechin with the Hartree–Fock (HF) method. The acidity for the C4′-OH group was reported as being slightly greater than that for the C3′-OH group. However, regarding a small difference in the deprotonation enthalpies (0.4–0.5 kcal mol^{-1}) reported for these two OH groups, reversion of the acidity order would be possible when using the more quantum mechanically accurate DFT method. As shown in Fig. 5, the highly negative value for the Gibbs energy of the proton transfer from O2 to O3 essentially indicates higher proton affinity of the oxygen atom at C4′ than the other at C3′. Hence, this supports the conclusion that the C4′-OH group is less acidic than the C3′-OH group.

3.6. Complexation of (+)-catechin with metal ions

Fig. 7 displays the optimized geometries for the complexes of (+)-catechin with Zn^{2+} and VO_2^+ in gas phase. In all cases, the ligand responsible for chelation is the tetra-anionic species $CatH^{4-}$, ensuring sufficiently high electron donation ability for the binding sites. For both types of metal ion, only one stable form of the complex has been found for M:L = 1:1, whereas there are two stable isomeric forms for M:L = 1:2. The Gibbs energies of complexation (ΔG_{comp}) are given in Table 5. Compared to the cases when M:L = 1:2, the complexation with M:L = 1:1 leads to the decrease in the ΔG_{comp} values by ~200 kcal mol^{-1} for either Zn^{2+} or VO_2^+. This indicates the most favorable complexation stoichiometry is M:L = 1:1 for both Zn^{2+} and VO_2^+. Previously, the stripping voltammetry experiment indicated that the complexation of Zn^{2+} with (+)-catechin in a pH 4.0 acetate aqueous–ethanol buffer preferred the 1:1 stoichiometry; however, the structure of the complex predicted therein with the semi-empirical method (ZINDO/1) could be inaccurate [57]. In contrast, the previous cyclic voltammetric study also suggested the formation of zinc(II) complex in dimethyl sulfoxide with mono-anionic (+)-catechin at the M:L ratio of 1:2 [58]. The spontaneous isomerization reactions **Zn2b** → **Zn2a** and **V2b** → **V2a** correspond to the Gibbs energy changes of −0.3 kcal mol^{-1} and −2.9 kcal mol^{-1}, respectively. Therefore, the isomers **Zn2b**/**Zn2a** are of comparable extent of formation while the degree of isomerization is much more important in the case of **V2b**/**V2a**. The magnitude of dipole moment in water is much greater for **Zn1** (57.4 Debye) than for **Zn2a** (0.22 Debye) or **Zn2b** (20.8 Debye), suggesting that the most favorable complex **Zn1** is highly compatible to polar solvents. The magnitude of dipole moment in water for the most favorable **V1** is quite similar to that for **V2a**, being close to 2/3 of the value for **V2b**.

The vibrational frequency calculations based on the DFT-optimized geometries of the complexes allow for the prediction of the infrared (IR) spectra, as displayed in Fig. 8a and b. Clearly, two isomers of the complex, i.e. **Zn2a**/**Zn2b** or **V2a**/**V2b**, give

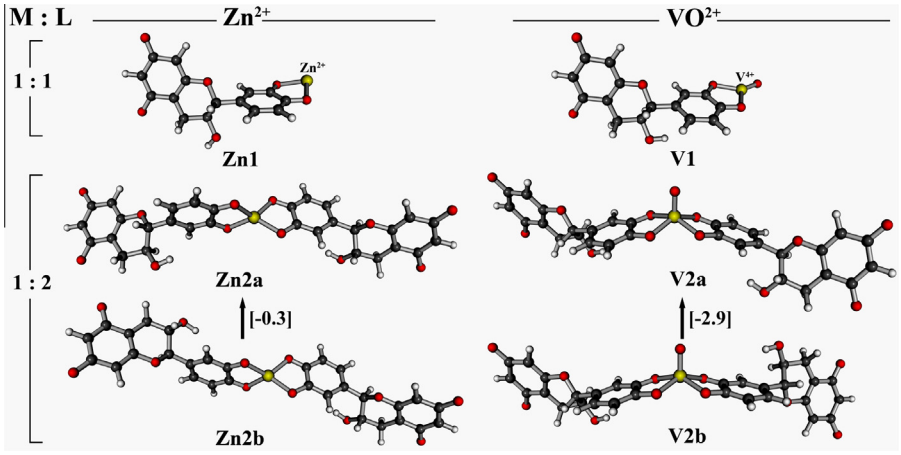

Fig. 7. Optimized geometries of the complexes formed by either Zn^{2+} or VO^{2+}, and the ligand $CatH^{4-}$ at different stoichiometric ratios. The Gibbs energies of isomerization (in kcal mol^{-1}): **Zn2b** → **Zn2a** and **V2b** → **V2a** are given in square brackets.

Table 5
Thermodynamic quantities for the possible complexation reactions of $CatH^{4-}$ with either Zn^{2+} or VO^{2+}, along with some molecular properties of the resulting complexes.

Complexation[a]	ΔE_{comp}[b]	ΔH_{comp}[b]	ΔG_{comp}[b]	Properties of complex				
				Absorption wavelength (nm)[c]	f[d]	Major electronic transitions	Dipole moment[e]	
							Gas phase	Aqueous phase
Zn^{2+} + L → **Zn1**	−871.4	−871.6	−863.7	369.0	0.0067	H → L+1 (77%) H → L+3 (21%)	10.7	57.4
				320.2	0.0063	H → L+5 (86%)		
Zn^{2+} + 2L → **Zn2a**	−676.6	−677.1	−654.6	286.2	0.1987	H-3 → L (34%) H-2 → L+1 (43%)	0.35	0.22
Zn^{2+} + 2L → **Zn2b**	−676.4	−676.8	−654.3	285.9	0.1728	H-3 → L+1 (42%) H-2 → L (27%) H-2 → L+2 (17%)	16.7	20.8
VO^{2+} + L → **V1a**	−910.2	−910.4	−899.9	547.4	0.0237	H-6 → L (34%) H-5 → L (36%) H-3 → L (28%)	8.87	11.6
VO^{2+} + 2L → **V2a**	−719.6	−720.4	−693.5	569.8	0.0033	H-10 → L+1 (27%) H-8 → L+1 (64%)	5.81	9.56
				368.6	0.0016	H-7 → L+2 (11%) H-4 → L (11%) H-4 → L+1 (27%) H-4 → L+2 (11%)		
VO^{2+} + 2L → **V2b**	−716.8	−717.7	−690.6	581.2	0.0042	H-10 → L+1 (19%) H-8 → L+1 (73%)	15.4	17.6
				366.9	0.0008	H-8 → L+2 (16%) H-8 → L+7 (31%)		

[a] L = the ligand $CatH^{4-}$.
[b] The values are given in kcal mol^{-1}.
[c] The values are obtained for the complex in water based on the IEFPCM(UAKS)/TD-DFT/B3LYP/6-311++G(d,p) calculations; the absorption maximum for $CatH^{4-}$ is found at 305 nm.
[d] The oscillator strength.
[e] The values are given in Debye.

almost identical IR spectral bands. However, for either Zn^{2+} or VO^{2+}, the complex with M:L = 1:1 shows distinguishing features compared to the corresponding complex with M:L = 1:2. In the IR spectrum of **Zn1** [Fig. 8a], three bands lying in between 2900 and 3060 cm^{-1} arise from different modes of C–H stretching on the ring C. The band at 3190 cm^{-1} is assigned to the C–H stretching at C8 on the ring A. The symmetric C–H stretching at C5′/C6′ on the ring B produces the strong band at 3160 cm^{-1}, with the shoulder near 3170 cm^{-1} caused by the C–H stretching at C6 on the ring A. The anti-symmetric C–H stretching at C5′/C6′ on the ring B also causes the band at 3134 cm^{-1}. For **Zn2a** and **Z2b** [Fig. 8a], the band at 3136 cm^{-1} is attributed to a combination of two C–H stretching modes at C2′ and C8. The bands due to the symmetric and anti-symmetric C–H stretching at C5′/C6′ on the ring B are both shifted to lower frequencies at 3115 and 3087 cm^{-1}, respectively. The band caused by the C–H stretching at C6 on the ring A is sharper and shifted to 3062 cm^{-1}. All bands due to the C–H stretching on the ring C are also shifted to the lower frequencies, lying in between 2880 and 3000 cm^{-1}. The markedly intense band at 2894 cm^{-1}, which is not found in the spectrum of **Zn1**, is due to the C–H stretching at C4 on the ring C. It is worth pointing that the C–H stretching bands at the frequencies higher than 2800 cm^{-1}, unfortunately, may be of little value in terms of characterization as they normally overlap with the strong and broad O–H stretching bands due to either the hydroxyl group or the presence of water in samples. In the lower-frequency range of 1200–1640 cm^{-1}, the bands for **Zn2a**/**Zn2b** are intense but broad, whereas for **Zn1** a greater number of narrow bands are observed. For **Zn1**, the aromatic C–C stretching on the ring B produces a band at 1600 cm^{-1} with quite low intensity. At the same frequency, the band for **Zn2a**/**Zn2b** shows higher intensity; however this band originates from the aromatic C–C stretching on the ring A rather than the ring B. The C–C stretching on the ring B for **Zn2a**/**Zn2b** only causes the shoulder near 1580 cm^{-1}. The intense band at 1568 cm^{-1} for **Zn1** is mainly due to the C–C stretching on both the rings B and A, coupled with the C–O stretching on the ring A. On the other hand, the intensity of such the band for **Zn2a**/**Zn2b** decreases dramatically due to the disappearance of vibrational contributions from the ring A. The other distinctive feature for **Zn2a**/**Zn2b** is, for example, the presence of a broad and strong band near 1500 cm^{-1} caused by several vibrational contributions: the strong CH_2 scissoring on the ring C, the moderate C–O stretching and the aromatic C–C stretching on the ring B, and the weak aromatic C–C stretching on the ring A. In the case of the **Zn1a** spectrum, this broad band is replaced by three closely lying narrow bands at 1520, 1496 and 1480 cm^{-1}, all with comparable intensity; they are assigned to the C–O stretching on the ring A, the C–O stretching coupled with the aromatic C–C stretching on the ring A, and the CH_2 scissoring on the ring C coupled with the C–O stretching on the ring A, respectively.

For the IR spectra of **V1** and the **V2a**/**V2b** isomers shown in Fig. 8b, a sharp and very strong band at 3064 cm^{-1} due to the C–H stretching at C4 on the ring C is invariant with the M:L ratio regarding its position. For **V1**, the relatively broad band at 3160 cm^{-1} arises from a combination of the C–H stretching at C6 on the ring A and the symmetric C–H stretching at C5′/C6′ on the ring B. The spectrum of **V1** in the region 1400–1640 cm^{-1} consists of several narrow bands whereas there are quite a few broad bands in the spectrum of **V2a**/**V2b** in the same frequency region. In the **V2a**/**V2b** spectra, the presence of the major broad band at 1500 cm^{-1} is ascribed to the CH_2 scissoring on the ring C coupled with the C–H bending on both the rings A and B. Upon changing the M:L ratio from 1:1 to 1:2, the intensity of the band near 1600 cm^{-1} increases immensely. This is due to the fact that for **V1** the band at such the position results from the C–C stretching on the ring B, but for **V2a**/**V2b** it is caused by the C–C stretching on the ring A instead. In the latter case, the band is also broadened due to the overlap with the weaker band emerging from the C–C stretching on the ring B. A wide separation between the strong bands at 1600 and 1504 cm^{-1} is clearly one of the most notable

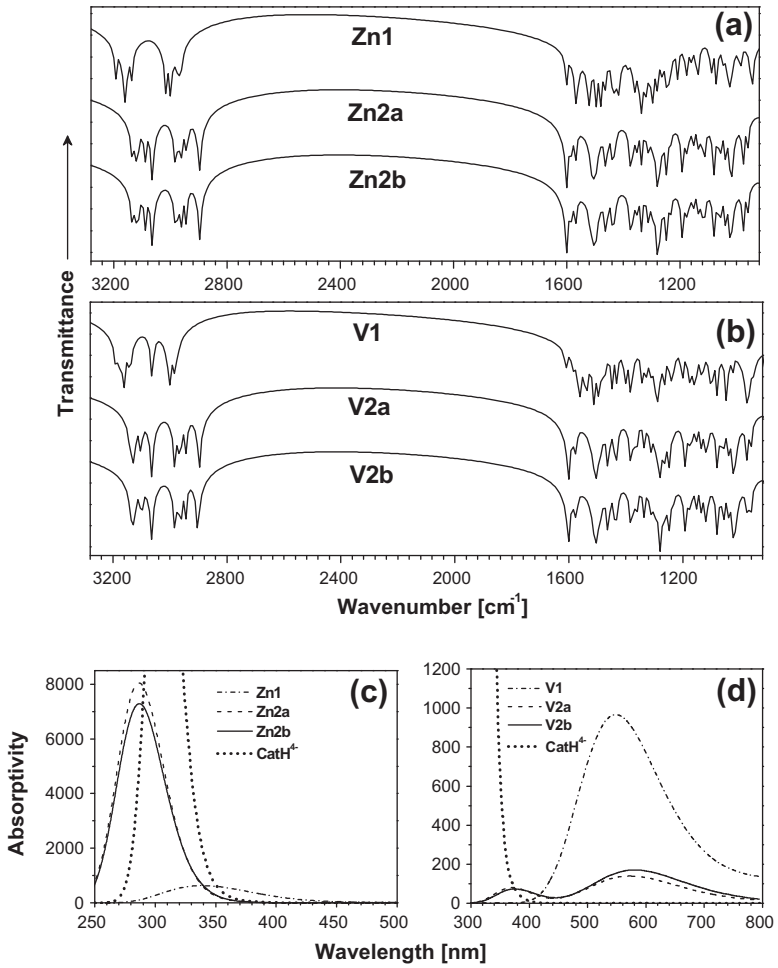

Fig. 8. Computed infrared spectra for the complexes of $CatH^{4-}$ with (a) Zn^{2+} and (b) VO^{2+}. Computed UV/visible spectra in water for the complexes of $CatH^{4-}$ with (c) Zn^{2+} and (d) VO^{2+}; the spectra of $CatH^{4-}$ are also included.

features for the **V2a**/**V2b** spectrum, similar to the observation on the **Zn2a**/**Zn2b** spectra. In the **V1** spectrum, the asymmetric band at 976 cm^{-1} is very intense and broad, resulting from the strong V–O stretching band at 967 cm^{-1} combined with the weak in-plane C–H bending on the rings A and B. The shoulder found at 960 cm^{-1} is mainly caused by the moderate in-plane C–H bending on the ring A. For **V2a**/**V2b**, the V–O stretching band is shifted to higher frequency at 1008 cm^{-1} so that it overlaps with the other C–H bending band to give the stronger band at 1024 cm^{-1}. Consequently, without the interference from the V–O stretching band, the C–H bending band at 976 cm^{-1} in the **V2a** spectrum becomes sharp and the resolution between this band and the adjacent band at 960 cm^{-1} is improved. Nonetheless, for **V2b**, the separation between these two bands is not much noticeable due to the decrease in the intensity of the band at 976 cm^{-1}.

The UV/visible absorption spectra in water of the complexes determined by the time-dependent DFT method, i.e., IEFPCM(UAKS)/TD-DFT/B3LYP/6-311++G(d,p), are shown in Fig. 8c and d. The wavelengths for the absorption maxima of these spectra along with the major electronic transitions for the complexes are reported in Table 5. Compared to the strong bands lying at ~286 nm for either **Zn2a** or **Zn2b**, the absorption band of **Zn1** is much weaker and located at the longer wavelength (369 nm). For the complexes of VO^{2+}, increasing molar proportion of the ligand in the molecule of the complex leads to the obvious reduction in the absorption intensity as well as the red-shift of the major absorption band. It is worth pointing that in the presence of free ligand, the absorption bands of the Zn^{2+} complexes would merge with the more intense band of the ligand in the same region. The visible-absorption bands of the VO^{2+} complexes are, in contrast, well separated from the band of the ligand, allowing more precise interpretation of the spectral data compared to the case of the Zn^{2+} complexes.

4. Conclusions

The most stable forms for the neutral and four deprotonated species of (+)-catechin determined with the IEFPCM(UAKS)/DFT/B3LYP/6-311++G(d,p) computational method exhibit fairly similar geometries. However, the changes in orbital interactions essentially lead to marked differences in the distribution of charge densities over the molecule. Electron delocalization over the rings A and B of (+)-catechin has been found to play a key role in stabilizing the conformations of the protonated species, most obviously for the neutral (+)-catechin and the mono-anionic species. Nevertheless, at the further steps of deprotonation, the conformational stabilization due to the other electronic effects such as the lone-pair electron donation from oxygen atoms to the rings and the intramolecular hydrogen bonding become increasingly important. The successive deprotonation also brings about the elevation of HOMO and LUMO levels for the (+)-catechin molecule and the resulting HOMO–LUMO gaps for the anionic species are smaller than the gap for the neutral species. Chemical instability is there-

fore predicted to increase upon deprotonation. Formation of both hydrogen and phenoxyl radicals is favored at high pH values regarding the decrease in the homolytic O–H bond dissociation enthalpy upon deprotonation. Also this may imply more effective radical scavenging activity for the deprotonated (+)-catechin species. Acidity of the OH groups on (+)-catechin decreases in the order: C3′-OH (ring B) > C5-OH (ring A) > C7-OH (ring A) > C4′-OH (ring B). The B–A–A–B ring sequence for the deprotonation is in good agreement with the previous experimental work by Slabbert [12]. The pK_a value at 9.3 determined for the most acidic OH group is also in satisfactory agreement with previous experimental data. However, the present theoretical predictions yield somewhat overestimated pK_a values for the less acidic OH groups, probably due to limited accuracy of the polarizable continuum model for charged species and/or the complex mechanism of the actual deprotonation events. The complexation of (+)-catechin with either zinc(II) or oxovanadium(IV) prefers the M:L ratio of 1:1. At such the mole ratio, one stable form of the complex is obtained for each type of metal ion. Due to the highly negative Gibbs energies of complexation, the complexation of (+)-catechin with oxovanadium(IV) is theoretically predicted to be more favorable than that with zinc(II); therefore, the chelation with the (+)-catechin ligand is more stable for oxovanadium(IV) than zinc(II) at the same stoichiometric ratio. Allowing for the M:L ratio of 1:2, the formation of two stable isomeric complexes is theoretically possible as well. These findings are not trivial as the pharmacological properties of a metal complex would vary with both isomeric structure and stoichiometry. In the study of complexation, since proton abstraction at the binding sites of the (+)-catechin ligand is assumed; therefore different results for the complexation might be obtained under acidic conditions, where the protonated species predominate. Nonetheless, it is reasonable to mention that protonation at the donor oxygen atoms could reduce the ability of electron donation to metal ion, to the extent that the metal chelation would be destabilized. As suggested by the computational data, the IR and UV/visible spectral information permits the stoichiometry identification of the (+)-catechin complexes for both types of metal ion; however, the presence of multiple forms of the complex in the real sample would complicate the spectra to some extent.

Acknowledgements

The authors are grateful to the Faculty of Science, Burapha University, Thailand and the Center of Excellence for Innovation in Chemistry (PERCH-CIC), Commission on Higher Education, Ministry of Education, Thailand for financial support.

References

[1] J.A. Ross, C.M. Kasum, Annu. Rev. Nutr. 22 (2002) 19–34.
[2] H. Tapiero, K.D. Tew, G.N. Ba, G. Mathe, Biomed. Pharmacother. 56 (2002) 200–207.
[3] J.V. Higdon, B. Frei, Crit. Rev. Food Sci. Nutr. 43 (2003) 89–143.
[4] S. de Pascual-Teresa, D.A. Moreno, C. Garcia-Viguera, Int. J. Mol. Sci. 11 (2010) 1679–1703.
[5] S. Mandel, M.B.H. Youdim, Free Radic. Biol. Med. 37 (2004) 304–317.
[6] M. Leopoldini, N. Russo, M. Toscano, Food Chem. 125 (2011) 288–306.
[7] M. Muzolf, H. Szymusiak, A. Gliszczyńska-Świgło, I.M. Rietjens, B. Tyrakowska, J. Agric. Food Chem. 56 (2008) 816–823.
[8] M. Muzolf-Panek, A. Gliszczynska-Swiglo, H. Szymusiak, B. Tyrakowska, Eur. Food Res. Technol. 235 (2012) 1001–1009.
[9] M. Kumamoto, T. Sonda, K. Nagayama, M. Tabata, Biosci. Biotechnol. Biochem. 65 (2001) 126–132.
[10] P. Janeiro, A.M. Oliveira Brett, Anal. Chim. Acta 518 (2004) 109–115.
[11] L. Khalafi, M. Rafiee, F. Yadaei, Res. Chem. Intermediat. 37 (2011) 1047–1055.
[12] N.P. Slabbert, Tetrahedron 33 (1977) 821–824.
[13] J.A. Kennedy, M.H.G. Munro, H.K.J. Powell, L.J. Porter, L.Y. Foo, Aust. J. Chem. 37 (1984) 885–892.
[14] J.M. Herrero-Martinez, M. Sanmartin, M. Roses, E. Bosch, C. Rafols, Electrophoresis 26 (2005) 1886–1895.
[15] C. Cren-Olivé, J.-M. Wieruszeski, E. Maes, C. Rolando, Tetrahedron Lett. 43 (2002) 4545–4549.
[16] C. Cren-Olivé, P. Hapiot, J. Pinson, C. Rolando, J. Am. Chem. Soc. 124 (2002) 14027–14038.
[17] H.F.P. Martins, J.P. Leal, M.T. Fernandez, V.H.C. Lopes, M. Cordeiro, J. Am. Soc. Mass Spectrom. 15 (2004) 848–861.
[18] R.A. Anderson, J. Am. Coll. Nutr. 17 (1998) 548–555.
[19] R.A. Anderson, Diabetes Metab. 26 (2000) 22–27.
[20] J.B. Vincent, Polyhedron 20 (2001) 1–26.
[21] N. Yasarawan, K. Thipyapong, S. Sirichai, V. Ruangpornvisuti, J. Mol. Struct. 1031 (2013) 144–151.
[22] Y. Yoshikawa, E. Ueda, H. Miyake, H. Sakurai, Y. Kojima, Biochem. Biophys. Res. Commun. 281 (2001) 1190–1193.
[23] H. Sakurai, Y. Kojima, Y. Yoshikawa, K. Kawabe, H. Yasui, Coord. Chem. Rev. 226 (2002) 187–198.
[24] Y. Yoshikawa, E. Ueda, K. Kawabe, H. Miyake, T. Takino, H. Sakurai, Y. Kojima, J. Biol. Inorg. Chem. 7 (2002) 68–73.
[25] Y. Adachi, J. Yoshida, Y. Kodera, A. Kato, Y. Yoshikawa, Y. Kojima, H. Sakurai, J. Biol. Inorg. Chem. 9 (2004) 885–893.
[26] H. Sakurai, Y. Adachi, Biometals 18 (2005) 319–323.
[27] M. Yamaguchi, K. Wakasugi, R. Saito, Y. Adachi, Y. Yoshikawa, H. Sakurai, A. Katoh, J. Inorg. Biochem. 100 (2006) 260–269.
[28] J. Jansen, W. Karges, L. Rink, J. Nutr. Biochem. 20 (2009) 399–417.
[29] G.R. Willsky, A.B. Goldfine, P.J. Kostyniak, J.H. McNeill, L.Q. Yang, H.R. Khan, D.C. Crans, J. Inorg. Biochem. 85 (2001) 33–42.
[30] H. Sakurai, Chem. Rec. 2 (2002) 237–248.
[31] K.H. Thompson, J. Lichter, C. LeBel, M.C. Scaife, J.H. McNeill, C. Orvig, J. Inorg. Biochem. 103 (2009) 554–558.
[32] H. Haase, W. Maret, Biometals 18 (2005) 333–338.
[33] W. Basuki, M. Hiromura, H. Sakurai, J. Inorg. Biochem. 101 (2007) 692–699.
[34] M. Badea, R. Olar, D. Marinescu, V. Uivarosi, V. Aldea, T.O. Nicolescu, J. Therm. Anal. Calorim. 99 (2010) 823–827.
[35] D. Malesev, V. Kuntic, J. Serb. Chem. Soc. 72 (2007) 921–939.
[36] M.J. Frisch, G.W. Trucks, H.B. Schlegel, G.E. Scuseria, M.A. Robb, J.R. Cheeseman, J.A. Montgomery, Jr., T. Vreven, K.N. Kudin, J.C. Burant, J.M. Millam, S.S. Iyengar, J. Tomasi, V. Barone, B. Mennucci, M. Cossi, G. Scalmani, N. Rega, G.A. Petersson, H. Nakatsuji, M. Hada, M. Ehara, K. Toyota, R. Fukuda, J. Hasegawa, M. Ishida, T. Nakajima, Y. Honda, O. Kitao, H. Nakai, M. Klene, X. Li, J.E. Knox, H.P. Hratchian, J.B. Cross, V. Bakken, C. Adamo, J. Jaramillo, R. Gomperts, R.E. Stratmann, O. Yazyev, A.J. Austin, R. Cammi, C. Pomelli, J.W. Ochterski, P.Y. Ayala, K. Morokuma, G.A. Voth, P. Salvador, J.J. Dannenberg, V.G. Zakrzewski, S. Dapprich, A.D. Daniels, M.C. Strain, O. Farkas, D.K. Malick, A.D. Rabuck, K. Raghavachari, J.B. Foresman, J.V. Ortiz, Q. Cui, A.G. Baboul, S. Clifford, J. Cioslowski, B.B. Stefanov, G. Liu, A. Liashenko, P. Piskorz, I. Komaromi, R.L. Martin, D.J. Fox, T. Keith, M.A. Al-Laham, C.Y. Peng, A. Nanayakkara, M. Challacombe, P.M.W. Gill, B. Johnson, W. Chen, M.W. Wong, C. Gonzalez, J.A. Pople, Gaussian 03, Revision C.02; Gaussian Inc., Wallingford, CT, 2004.
[37] A.D. Becke, J. Chem. Phys. 98 (1993) 5648–5652.
[38] C. Lee, W. Yang, R.G. Parr, Phys. Rev. B 37 (1988) 785–789.
[39] M. Caricato, B. Mennucci, J. Tomasi, F. Ingrosso, R. Cammi, S. Corni, G. Scalmani, J. Chem. Phys. 124 (2006) 124520–124532.
[40] S. Sun, W. Chen, W. Cao, F. Zhang, J. Song, C. Tian, J. Mol. Struct. (THEOCHEM) 860 (2008) 40–44.
[41] D.M. Camaioni, C.A. Schwerdtfeger, J. Phys. Chem. A 109 (2005) 10795–10797.
[42] M.D. Tissandier, K.A. Cowen, W.Y. Feng, E. Gundlach, M.H. Cohen, A.D. Earhart, J.V. Coe, T.R. Tuttle, J. Phys. Chem. A 102 (1998) 7787–7794.
[43] C.P. Kelly, C.J. Cramer, D.G. Truhlar, J. Phys. Chem. B 110 (2006) 16066–16081.
[44] K.S. Alongi, G.C. Shields, Ann. Rep. Comput. Chem. 6 (2010) 113–138.
[45] M.D. Liptak, K.C. Gross, P.G. Seybold, S. Feldgus, G.C. Shields, J. Am. Chem. Soc. 124 (2002) 6421–6427.
[46] D.A. McQuarrie, Statistical Mechanics, University Science Books, Mill Valley, CA, 1973.
[47] M.D. Liptak, G.C. Shields, J. Am. Chem. Soc. 123 (2001) 7314–7319.
[48] M.T. Fernandez, M.L. Mira, M.H. Florêncio, K.R. Jennings, J. Inorg. Biochem. 92 (2002) 105–111.
[49] M. Leopoldini, N. Russo, S. Chiodo, M. Toscano, J. Agric. Food Chem. 54 (2006) 6343–6351.
[50] J. Ren, S. Meng, C.E. Lekka, E. Kaxiras, J. Phys. Chem. B 112 (2008) 1845–1850.
[51] N.M. O'Boyle, A.L. Tenderholt, K.M. Langner, J. Comput. Chem. 29 (2008) 839–845.
[52] R.G. Pearson, J. Chem. Sci. 117 (2005) 369–377.
[53] R.G. Parr, R.G. Pearson, J. Am. Chem. Soc. 105 (1983) 7512–7516.
[54] V. Barone, M. Cossi, J. Phys. Chem. A 102 (1998) 1995–2001.
[55] M. Mangold, L. Rolland, F. Costanzo, M. Sprik, M. Sulpizi, J. Blumberger, J. Chem. Theor. Comput. 7 (2011) 1951–1961.
[56] M. Sulpizi, M. Sprik, J. Phys.: Condens. Matter 22 (2010) 2841161–2841168.
[57] I. Esparza, I. Salinas, C. Santamaria, J.M. Garcia-Mina, J.M. Fernandez, Anal. Chim. Acta 543 (2005) 267–274.
[58] M.E. Bodini, M.A. del Valle, R. Tapia, F. Leighton, P. Berrios, Polyhedron 20 (2001) 1005–1009.